Scaling law for transition probabilities in $2p^3$ configuration from LS coupling to jj coupling

Xiao-Ying Han,[1,*] Xiang Gao,[2,†] De-lin Zeng,[3] Rui Jin,[4] Jun Yan,[1] and Jia-Ming Li[3,4,5]

[1]*Institute of Applied Physics and Computational Mathematics, Beijing 100088, China*

[2]*Beijing Computational Science Research Center, Beijing 100084, China*

[3]*Key Laboratory for Laser Plasmas (Ministry of Education) and Department of Physics and Astronomy, Shanghai Jiao Tong University, Shanghai 200240, China*

[4]*Department of Physics and Center for Atomic and Molecular Nanosciences, Tsinghua University, Beijing 100084, China*

[5]*Collaborative Innovation Center of Quantum Matter, Beijing 100084, China*

(Received 2 October 2013; revised manuscript received 14 January 2014; published 29 April 2014)

The $E2$ and $M1$ transition rates among the lowest five states ($[^4S^o_{3/2}]'$,$[^2D^o_{5/2}]'$,$[^2D^o_{3/2}]'$,$[^2P^o_{3/2}]'$,$[^2P^o_{1/2}]'$), i.e., the $[^2D^o_{5/2,3/2}]' \rightarrow [^4S^o_{3/2}]'$ and $[^2P^o_{3/2,1/2}]' \rightarrow [^4S^o_{3/2}]'$ transitions, in the $2p^3$ configuration of a nitrogenlike isoelectronic sequence (from $Z = 7$ to $Z = 79$) are calculated by using a large-scale multiconfiguration Dirac-Fock method. The scaling laws of the excitation energies, fine-structure splittings, forbidden transition rates, line strengths, and ratios of line intensities varying with Z are investigated. The underlying physical mechanism leading to the change of the scaling laws from low Z to high Z are discussed. The calculated transition probabilities and scaling laws are expected to be useful for astrophysical and plasma physical applications.

DOI: 10.1103/PhysRevA.89.042514 PACS number(s): 31.15.am, 31.30.jc, 32.70.Fw

I. INTRODUCTION

The transitions $[^2D^o_{5/2,3/2}]' \rightarrow [^4S^o_{3/2}]'$ and $[^2P^o_{3/2,1/2}]' \rightarrow [^4S^o_{3/2}]'$ in the $2p^3$ configuration for a nitrogenlike isoelectronic sequence are forbidden for electric dipole ($E1$) radiation because of the same odd parity of the initial and final states, but they are allowed for electric quadrupole ($E2$) and magnetic dipole ($M1$) radiations. Here $[^4S^o_{3/2}]'$,$[^2D^o_{5/2}]'$,$[^2D^o_{3/2}]'$,$[^2P^o_{3/2}]'$, and $[^2P^o_{1/2}]'$ represent the five lowest states of the $2p^3$ configuration, for which LS coupling is appropriate at low Z while jj coupling is appropriate at high Z. The accurate atomic data, e.g., the energy levels and transition probabilities, of the nitrogenlike isoelectronic sequence play an important role in astrophysical and plasma physics [1,2]. For example, in planetary nebulas (PNs), the ratio of forbidden line intensities of $[^2D^o_{5/2,3/2}]' \rightarrow [^4S^o_{3/2}]'$ transitions provides much valuable astrophysical information for density diagnostics when good observation is combined with high-quality atomic data [1]. The forbidden lines of Mg^{5+}, Si^{7+}, and S^{9+} can be used to diagnose the electron densities in the inner corona [3]; the forbidden lines of higher ionized atoms, such as Ti^{15+} and Fe^{19+}, are very useful for fusion plasma diagnostics [4].

Since it is difficult to experimentally provide the atomic data for these forbidden line intensities of the isoelectronic sequence in a terrestrial laboratory, a great deal of theoretical efforts have been devoted to provide the atomic data. For example, Zeippen [5] calculated transition probabilities for all forbidden lines in the $2p^3$ configuration from $Z = 7$ to $Z = 26$ for the nitrogenlike isoelectronic sequence by using the SUPERSTRUCTURE code [6] with a Breit-Pauli relativistic correction to the nonrelativistic Hamiltonian. This work made an improvement in the astrophysically needed atomic data through a set of more expanded orbital bases up to $4s$ as well as improved electron correlations, excitation energy corrections, and corrections to the magnetic dipole operators compared with previous works [7–12]. Then, following the development of the computational resources, Fischer and Tachiev [13] reported their calculated forbidden line intensities for the same isoelectron sequence from $Z = 7$ to $Z = 11$ by using the multiconfiguration Hartree-Fock (MCHF) method [14] with relativistic effects included through the Breit-Pauli (BP) Hamiltonian based on orbital bases up to $7g$. Recently, Wang *et al.* [15] calculated the energy levels of the $2p^3$ configuration along the sequence from $Z = 7$ to $Z = 100$ with a fully relativistic multiconfiguration Dirac-Fock (MCDF) method based on a set of orbital bases up to $n = 7$. Chen *et al.* [16] and Han *et al.* [17] reported the ratio of $[^2D^o_{5/2,3/2}]' \rightarrow [^4S^o_{3/2}]'$ transitions for O II by using a large-scale fully relativistic MCDF method including the quantum electrodynamic (QED) corrections as perturbations based on the orbital bases up to $n = 7$ and $n = 9$, respectively. Particularly, the calculations of Ref. [17] take into account large-scale electron correlations (including the valence- and core-excitation correlations) within the "quasicomplete" basis scenario; thus the convergence happens in a systematical and uniform manner, and a better convergence is achieved.

Motivated, on the one hand, by the application requirement for updating atomic data, in this work, we calculate the $E2$ and $M1$ transition rates of $[^2D^o_{5/2,3/2}]' \rightarrow [^4S^o_{3/2}]'$ and $[^2P^o_{3/2,1/2}]' \rightarrow [^4S^o_{3/2}]'$ transitions of a N-like isoelectronic sequence from $Z = 7$ to $Z = 79$ by using a large-scale fully relativistic MCDF method based on a set of quasicomplete bases. On the other hand, we note that previous works [15,18–20], which investigated the dependence of the relativistic effect of the isoelectronic sequence on Z, mainly focused on the energy levels. However, for a many-electron atomic system, especially for a forbidden transition within the same configuration, the dependence of the transition probabilities on Z has not been well known in a quantitative way up to now. In this work, based on our systematically convergent calculation results, the scaling laws of the transition energies, fine-structure energy splittings, and forbidden $E2$ and $M1$ transition rates of the

*han_xiaoying@iapcm.ac.cn

†xgao@csrc.ac.cn

$[^2D^o_{5/2,3/2}]' \rightarrow [^4S^o_{3/2}]'$ and $[^2P^o_{3/2,1/2}]' \rightarrow [^4S^o_{3/2}]'$ transitions are determined. Along with the evolution of the above physical quantities with Z, some interesting features, e.g., the change in the scaling law, are found. In general, these features reflect the competitions between the spin-orbit interactions and the electron-electron interactions.

II. THEORETICAL METHOD

Since detailed descriptions of the MCDF method have been presented elsewhere [21–25], a brief outline will be given here. The interactions in a many-electron atomic system can be separated into two types: longitudinal and transverse interactions. In the Coulomb gauge, the atomic Hamiltonian with only the longitudinal electron-nucleus and electron-electron interactions can be expressed as (atomic units are used throughout the paper if not otherwise specified)

$$H_{DC} = \sum_i \left[c\vec{\alpha} \cdot \vec{p}_i + (\beta + 1)c^2 - \frac{Z}{r_i} \right] + \sum_{i<j} \frac{1}{\vec{r}_i - \vec{r}_j}. \quad (1)$$

The transverse interactions and the interactions with radiation fields are treated as perturbations. Based on the Dirac-Coulomb Hamiltonian given in Eq. (1), the atomic state functions (ASFs), $|\Gamma P J M\rangle$, can be calculated by solving the following equation:

$$H_{DC}|\Gamma P J M\rangle = E_\Gamma |\Gamma P J M\rangle, \quad (2)$$

where P is the parity and J and M are the total angular momentum and magnetic quantum number, respectively. Γ denotes the Γth atomic eigenstate function. The ASFs are N-electron eigenstate wave functions, which are linear combinations of configuration state functions (CSFs) with the same P, J, and M, namely,

$$|\Gamma P J M\rangle = \sum_{r=1}^{n_c} C_{r\Gamma} |\gamma_r P J M\rangle, \quad (3)$$

where $C_{r\Gamma}$ is the expansion coefficient and γ_r represents all other information to define the CSF uniquely. The CSFs, $|\gamma_r P J M\rangle$, which form a quasicomplete basis set for an N-electron atomic system in Hilbert space, are linear combinations of Slater determinants of atomic orbital wave functions (AOs). By applying the variational method to solve Eq. (2), we can obtain the mixing coefficients $C_{r\Gamma}$ as well as the AOs self-consistently. The quality of the AOs is extremely crucial to the final extensive configuration interaction (CI) calculations. Many works have illustrated procedures to obtain a set of AO bases, such as the single-configuration Dirac-Fock method [26], the B-spline method [27], and the MCDF method [28–35]. The MCDF method was proved to be a very powerful one. Many computer packages are developed to carry out MCDF calculations. GRASP92 [21] and an updated version, GRASP2K [22], are the most successful ones.

On the other hand, it is known that performing the MCDF calculation is not a straightforward procedure using the GRASP codes. For example, the configurations adopted in the calculations must be judiciously chosen. We have investigated how to guarantee the convergence of the multiconfiguration self-consistent-field (MCSCF) calculations systematically by using the quasicomplete basis scenario [36]. In brief, we call the basis which satisfies the desired accuracy of calculations a quasicomplete basis, which consists of spectroscopic orbitals (with $n - l - 1$ nodes) and pseudo-orbitals (without fixed nodes). Based on the GRASP2K codes, we developed the GRASP-JT edition to implement our calculation scenario automatically. Some auxiliary programs are developed to streamline the whole calculation. In order to guarantee the properties required by our quasicomplete basis definitions, the specific configurations used in the optimization processes of the spectroscopic orbitals and pseudo-orbitals are generated based on our previous MCDF calculation experience implemented in various atomic systems [17,36–40]. More specifically, the construction of our calculations can be divided into the following three main steps. The first step is to prepare the spectroscopy orbitals by optimizing the main physical states. The spectroscopic orbitals are used to represent the main physical states, whose quantum defects should have channel properties according to the quantum defect theory; that is, the quantum defects of the orbitals in an eigenchannel should be a smooth function of the excitation energy. To achieve this, the quantum defects of these orbitals are extracted from the calculations and are used as an important criterion for the convergence. The configurations for the N-electron system used to obtain the spectroscopy orbitals are generated by a single excitation from the key configurations. The second step is to prepare the pseudo-orbitals based on the fixed spectroscopic orbitals. Note that the character of the spectroscopy orbitals influences the optimization of the pseudo-orbitals. The pseudo-orbitals are used to deal with the important electron correlations, involving the monopole, dipole, and some quadrupole dynamical correlations. The effects of the limited pseudo-orbitals in the CI calculation are very close to the full CI result using the infinite configurations of the whole Hilbert space. Therefore the pseudo-orbitals can be viewed as a specific linear combination of infinite-bound-type Rydberg orbitals and continuum orbitals. To avoid the failure of the self-consistency optimization procedure, the configurations in the optimization are chosen according to the multipole expansion of $1/r_{12}$, i.e., monopole, dipole, and so on. More specifically, the configurations adopted in the former step are taken as reference configurations here. Given the information about the active electrons as an input, an analysis of these reference configurations is carried out in order to generate all of the monopole and dipole polarization of the active electrons. Note that, from the definition of the MCSCF calculation, our pseudo-orbital bases are a subset of the correlation orbitals in Refs. [28–35], which are obtained by choosing more configurations in the optimization. Finally, the third step is a large-scale CI calculation, i.e., calculating the energy levels and transition probabilities based on the quasicomplete bases using the same RCI program as in the GRASP2K codes. The configurations adopted are generated by the single, double, and some higher excitations from the key configurations in the first step, through which all of the monopole, dipole, and important quadrupole polarization correlations can be considered. By using our GRASP-JT codes, it may be easier to get a systematical convergence for the atomic structure calculations, especially for the present case of forbidden transition rate calculations. For example, the convergence of Chen's calculation [16] for the forbidden transitions of O II using the GRASP2K codes is

TABLE I. The transformation matrix between the two sets of CSFs arising from the $2p^3$ configuration by *LS* coupling and *jj* coupling [43].

	$\mathrm{CSF}^{(A)}_{\{LSj\}}:{}^4S^o_{3/2}$	$\mathrm{CSF}^{(B)}_{\{LSj\}}:{}^2D^o_{5/2}$	$\mathrm{CSF}^{(C)}_{\{LSj\}}:{}^2D^o_{3/2}$	$\mathrm{CSF}^{(D)}_{\{LSj\}}:{}^2P^o_{3/2}$	$\mathrm{CSF}^{(E)}_{\{LSj\}}:{}^2P^o_{1/2}$
$\mathrm{CSF}^{(a)}_{\{jj\}}:[(2p^2_{1/2})_0(2p^1_{3/2})_{3/2}]J^\pi=3/2^o$	$\sqrt{2}/3$	0	$-\sqrt{5/18}$	$1/\sqrt{2}$	0
$\mathrm{CSF}^{(b)}_{\{jj\}}:[(2p^1_{1/2})_{1/2}(2p^2_{3/2})_2]J^\pi=5/2^o$	0	1	0	0	0
$\mathrm{CSF}^{(c)}_{\{jj\}}:[(2p^1_{1/2})_{1/2}(2p^2_{3/2})_2]J^\pi=3/2^o$	$\sqrt{5}/3$	0	$2/3$	0	0
$\mathrm{CSF}^{(d)}_{\{jj\}}:[(2p^3_{3/2})_{3/2}]J^\pi=3/2^o$	$-\sqrt{2}/3$	0	$\sqrt{5/18}$	$1/\sqrt{2}$	0
$\mathrm{CSF}^{(e)}_{\{jj\}}:[(2p^1_{1/2})_{1/2}(2p^2_{3/2})_0]J^\pi=1/2^o$	0	0	0	0	1

not in a uniform manner. However, our previous calculations of O II [17] using the GRASP-JT codes surpass the precision of Chen's, and the convergent behavior is in a uniform manner.

In this work we implement the quasicomplete basis scenario to calculate all the relevant AO bases. More specifically, the AOs with principal quantum numbers $n=1,2$ are optimized together by MCSCF iterations to minimize the statistic weight summation $\mathcal{F}$ of the lowest five energy levels $([^4S^o_{3/2}]',[^2D^o_{5/2,3/2}]',[^2P^o_{3/2,1/2}]')$ of the $2p^3$ configuration. Here the multiconfigurations are generated by single ($\mathcal{S}$) and double ($\mathcal{D}$) electron excitations from the reference configuration $1s^22s^22p^3$. The AOs with $n=1,2$ are spectroscopic orbital bases. The AOs with $n=1,2$ are fixed, and the AOs with $n=3$ are obtained by MCSCF iterations to optimize the same $\mathcal{F}$, where the configurations are generated by $\mathcal{S}$ and $\mathcal{D}$ electron excitations from the reference configurations $2p^3$ and $2p^23p$ to all the AOs with $n=2,3$ and $l=0,\ldots,n-1$ (namely, the occupation number of the $1s$ orbital of all the configurations is fixed to be 2). In succession, once the AOs ($n\leqslant 3$) are fixed, the AOs are extended to $n_{\max}$ from n to $n+1$ by optimizing $\mathcal{F}$ with the multiconfigurations generated by $\mathcal{S}$ and $\mathcal{D}$ electron excitations from the reference configurations $2p^3$ and $2p^23p$ to the AOs with $n=2,\ldots,n_{\max}$ and $l=0,\ldots,\min(n_{\max}-1,7)$. None of the nodes of AOs with $n\geqslant 3$ are fixed, and they are expected to be pseudostate orbitals. We note that for higher Z, the calculation results converge faster; namely, for higher Z a smaller $n_{\max}$ can guarantee the convergence of the calculations. Thus for $Z\leqslant 10$ we adopt $n_{\max}=9$, while for $Z>10$ we adopt $n_{\max}=7$.

Based on the AOs, all sorts of physical values are calculated with the CI method, including the $\mathcal{S}$ and $\mathcal{D}$ electron excitation configurations from the reference configuration $1s^22s^22p^3$, which means the core ($1s^2$) and valence ($2s^22p^3$) are all relaxed. So the valence- and core-excitation correlations are all taken into account, which is important for convergence. The QED corrections, especially the Breit interaction, are added to the atomic Hamiltonian as a perturbation in the CI calculations. The Breit interaction is the most important high-order correction not only for the energy levels but also for the transition rates. The Breit (transverse) interaction represents the relativistic retardation effect of electromagnetic interactions with the finite velocity of light [41,42], especially the retarded magnetic interactions among the electron currents [26]. In our calculations the results considering the Breit interaction and the other QED effects are nearly equal to the results considering only the Breit interaction, and generally, their difference is only about one in a thousand or even less; thus in the following we present only the calculation results considering the Breit interaction.

III. RESULTS AND DISCUSSIONS

Table I shows the transformation matrix between the two sets of CSFs arising from the $2p^3$ configuration by LS coupling and jj coupling [43]. Table II shows our calculated square of the expansion coefficients $C_{r\Gamma}$ based on these two sets of CSFs for the lowest five states of the $2p^3$ configuration for the N atom and Au^{72+} ion. It can be seen that for the N atom the mixing among the set of $\mathrm{CSF}_{\{LSj\}}$ is weak and that the LS coupling is a good coupling scheme since the electron-electron interactions are dominant at low Z, while for the Au^{72+} ion the mixing in the set of $\mathrm{CSF}_{\{jj\}}$ is weak and the jj coupling is an appropriate choice since the relativistic effects are dominant at high Z. The competition between the relativistic effects, mainly the spin-orbit interactions, and the electron-electron interactions leads to some interesting changes in the dependence of the energy

TABLE II. The square of expansion coefficients for the lowest five levels in $2p^3$ configurations for the N atom and Au^{72+} ion expanded by $\mathrm{CSF}_{\{jj\}}$ and $\mathrm{CSF}_{\{LSj\}}$ (listed in Table I).

	State	$\mathrm{CSF}^{(a)}_{\{jj\}}$	$\mathrm{CSF}^{(b)}_{\{jj\}}$	$\mathrm{CSF}^{(c)}_{\{jj\}}$	$\mathrm{CSF}^{(d)}_{\{jj\}}$	$\mathrm{CSF}^{(e)}_{\{jj\}}$	Others	$\mathrm{CSF}^{(A)}_{\{LSj\}}$	$\mathrm{CSF}^{(B)}_{\{LSj\}}$	$\mathrm{CSF}^{(C)}_{\{LSj\}}$	$\mathrm{CSF}^{(D)}_{\{LSj\}}$	$\mathrm{CSF}^{(E)}_{\{LSj\}}$	Others
N	$[^4S^o_{3/2}]'$	0.2154		0.5339	0.2117		0.0390	0.9610					0.0390
	$[^2D^o_{5/2}]'$		0.9583				0.0417		0.9583				0.0417
	$[^2D^o_{3/2}]'$	0.2731		0.4259	0.2593		0.0417			0.9582			0.0418
	$[^2P^o_{3/2}]'$	0.4585			0.4759		0.0656				0.9344		0.0656
	$[^2P^o_{1/2}]'$					0.9345	0.0655					0.9345	0.0655
Au^{72+}	$[^4S^o_{3/2}]'$	0.9994					0.0006	0.2347		0.2742	0.4908		0.0004
	$[^2D^o_{5/2}]'$		0.9998				0.0002		0.9998				0.0002
	$[^2D^o_{3/2}]'$			0.9996			0.0002	0.5547		0.4449			0.0004
	$[^2P^o_{3/2}]'$				0.9939		0.0061	0.2097		0.2797	0.5047		0.0059
	$[^2P^o_{1/2}]'$					0.9994	0.0006					0.9994	0.0006

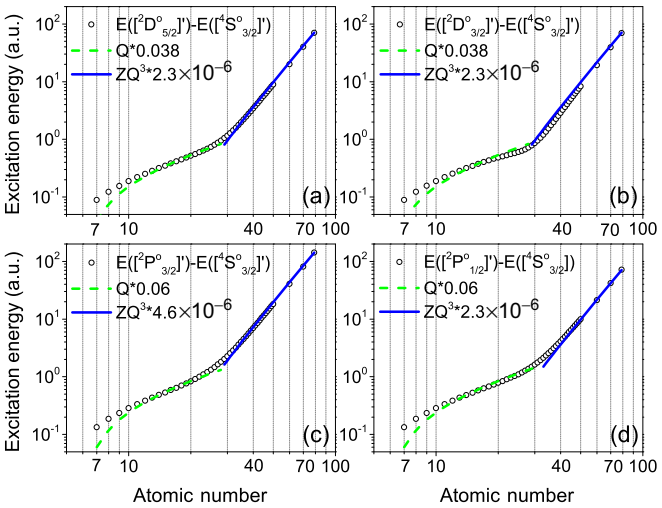

FIG. 1. (Color online) The scaling law of the energy difference for a N-like isoelectronic sequence. (a) For the $[^2D^o_{5/2}]' \rightarrow [^4S^o_{3/2}]'$ transition. (b) For the $[^2D^o_{3/2}]' \rightarrow [^4S^o_{3/2}]'$ transition. (c) For the $[^2P^o_{3/2}]' \rightarrow [^4S^o_{3/2}]'$ transition. (d) For the $[^2P^o_{1/2}]' \rightarrow [^4S^o_{3/2}]'$ transition.

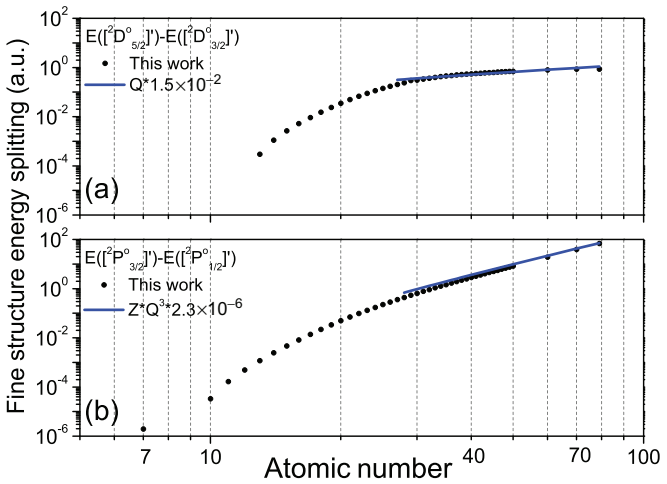

FIG. 2. (Color online) The scaling law of the fine-structure energy splittings in the high-Z region for $[^2D^o_{5/2,3/2}]'$ and $[^2P^o_{3/2,1/2}]'$ states.

levels and transition probabilities on Z, which are investigated in the following.

Scaling law for energy. Figure 1 shows the excitation energies of the four excited states $[^2D^o_{5/2,3/2}]'$ and $[^2P^o_{3/2,1/2}]'$ relative to the lowest state $[^4S^o_{3/2}]'$ of the $2p^3$ configuration from $Z = 7$ to $Z = 79$. It is easy to see that the excitation energies can be divided into roughly two parts, and each part has a different scaling law.

More specifically, in the high-Z region (roughly corresponding to $Z > 28$), the excitation energy can be scaled by ZQ^3, where $Q = Z - 6$ is the effective nuclear charge number which makes Q equal to unity for a neutral N atom. In this high-Z region, the relativistic effects, mainly the spin-orbit interactions ($\frac{\alpha^2 Z}{2}\frac{l\cdot\mathbf{s}}{r^3}$, where α is the fine-structure constant), are dominant compared with the electron-electron interactions; thus the energy difference of $2p_{1/2}$ and $2p_{3/2}$ is proportional to ZQ^3, where the relation $r \propto Q^{-1}$ [44] is used. Therefore the excitation energy of the four excited states $[^2D^o_{5/2,3/2}]'$ and $[^2P^o_{3/2,1/2}]'$ is proportional to $\Delta q Z Q^3$, where Δq is the excited electron number from $2p_{1/2}$ to $2p_{3/2}$ orbitals in the chief $\mathrm{CSF}_{\{jj\}}$ for the four excited states compared with the ground state. Note that the excitation energies of $[^2D^o_{5/2,3/2}]'$ and $[^2P^o_{1/2}]'$ states are half of those of the $[^2P^o_{3/2}]'$ state at the same Z. The reason for the double relation is that Δq for $[^2D^o_{5/2,3/2}]'$ and $[^2P^o_{1/2}]'$ states are all 1, while Δq for $[^2P^o_{3/2}]'$ state is 2, as shown through the combination of Tables I and II.

In Fig. 1, in the low-Z region (roughly corresponding to $Z < 28$) the excitation energy is scaled by Q. This is due to the dominant electron-electron interactions. We can estimate that at $Z = 28$, the electron-electron interactions (described by $1/r_{12}$ and scaled by Q) $\sim Q$ (≈ 22) are larger than the spin-orbit interactions $\sim ZQ^3\alpha^{-2}$ (≈ 16). With decreasing Z, $ZQ^3\alpha^{-2}$ decreases faster than Q. Thus in the low-Z region the excitation energy follows the scaling law of Q. From the high-Z region to the low-Z region, the change of the scaling law for excitation energy illustrates the competition between the spin-orbit interactions and the electron-electron interactions. At the lower Z, e.g., corresponding to $Z < 13$, the electron-electron interactions become more complicated; therefore the scaling law deviates Q and approaches $Q^{0.6}$.

Figure 2 shows the fine-structure splittings of $[^2D^o_{5/2,3/2}]'$ and $[^2P^o_{3/2,1/2}]'$ states. From Tables I and II, we can see that the difference of the chief $\mathrm{CSF}_{\{jj\}}$ for $[^2D^o_{5/2}]'$ and $[^2D^o_{3/2}]'$ states is only the coupling coefficient between the $2p_{1/2}$ and $2p_{3/2}$ orbitals. The different coupling coefficient reflects the different space distances between the electrons in the $2p_{1/2}$ and $2p_{3/2}$ orbitals, which means the different electron-electron interactions. Thus the splitting of $[^2D^o_{5/2,3/2}]'$ is scaled by Q in the high-Z region. For $[^2P^o_{3/2}]'$ and $[^2P^o_{1/2}]'$ states, the dominant difference of the chief $\mathrm{CSF}_{\{jj\}}$ is the occupation number of the $2p_{1/2}$ and $2p_{3/2}$ orbitals; thus their splitting is scaled by ZQ^3 in the high-Z region. In the low-Z region, the fine-structure splittings are small and sensitive to the subtle competition between the Breit and spin-orbit interactions and are difficult to scale by a simple analytical law.

For $[^2D^o_{5/2,3/2}]'$ states, our calculated fine-structure splittings at $Z = 7$–26 agree with the experimental values [45] within a few percent. In general, our theoretical results agree better with the experimental measurements than the theoretical results of Ref. [5] and agree with the theoretical results of Ref. [13] within 4% except for Na^{4+}, which is within ~9%. For $[^2P^o_{3/2,1/2}]'$ states, our calculated fine-structure splittings agree with the experimental values [45] by about 2% for $Z = 13$–26. For $Z < 13$, since the absolute values of the splittings are tiny ($\sim 10^{-6}$), the convergence is difficult, and our theoretical results differ from the experimental values by several tens of percent. The theoretical results of Ref. [5] and our theoretical results are in an agreement within 7% for $Z = 11$–26, while for $Z = 7$–10 the difference is from 20% to 80%. For $Z = 7$–10 our results differ from the results of Ref. [13] by magnitude, while for $Z = 11$ the two theoretical results agree within about 2%.

Scaling law for transition rate and line strength. Table III shows the scaling law for the electric (E^λ) and magnetic

TABLE III. The scaling law for the excitation energy, the multipole (λ) transition rate, and the corresponding line strength S.

Multipole fields	Coupling	Transition rate[a]	Scaling law for ΔE	Scaling law for rate	Scaling law for S
Electric multipole (λ)	Charge coupling (major)	$\propto \Delta E^{2\lambda+1}(r^{\lambda})^2$	$\propto Z\,Q^3$ (for high Z)	$\propto Z^{2\lambda+1}\,Q^{4\lambda+3}$	$\propto Q^{-2\lambda}$
			$\propto Q$ (for low Z)	$\propto Q$	$\propto Q^{-2\lambda}$
	Magnetic momentum coupling (minor)	$\propto \Delta E^{2\lambda+1}(r^{\lambda}\Delta E)^2$	$\propto Z\,Q^3$ (for high Z)	$\propto Z^{2\lambda+3}\,Q^{4\lambda+9}$	$\propto Z^2\,Q^{-2\lambda+6}$
			$\propto Q$ (for low Z)	$\propto Q^3$	$\propto Q^{-2\lambda+2}$
Magnetic multipole (λ)	Magnetic momentum coupling (major)	$\propto \Delta E^{2\lambda+1}(r^{\lambda-1})^2$	$\propto Z\,Q^3$ (for high Z)	$\propto Z^{2\lambda+1}\,Q^{4\lambda+5}$	$\propto Q^{-2\lambda+2}$
			$\propto Q$ (for low Z)	$\propto Q^3$	$\propto Q^{-2\lambda+2}$
	Charge coupling (minor)	$\propto \Delta E^{2\lambda+1}(r^{\lambda+1}\Delta E)^2$	$\propto Z\,Q^3$ (for high Z)	$\propto Z^{2\lambda+3}\,Q^{4\lambda+7}$	$\propto Z^2\,Q^{-2\lambda+4}$
			$\propto Q$ (for low Z)	$\propto Q$	$\propto Q^{-2\lambda}$

[a]Readers can consult Ref. [46] for details, and a concise description is given in the Appendix.

(M^{λ}) multipole transition rates derived from the nonrelativistic Hamiltonian in a single-particle model approximation, as shown in detail in Ref. [46]; a concise description is given in the Appendix. Here the scaling law of excitation energy ΔE is from Fig. 1.

For $E2$ ($\lambda = 2$) and $M1$ ($\lambda = 1$) transitions, the relation between the rate A_{ij} (in s^{-1} unit) and line strength S_{ij} is given by [5]

$$A_{ij}(E2) = 2.6733 \times 10^3 \times (E_i - E_j)^5 \frac{1}{g_i} S_{ij}^{E2}, \tag{4}$$

$$A_{ij}(M1) = 3.5644 \times 10^4 \times (E_i - E_j)^3 \frac{1}{g_i} S_{ij}^{M1}, \tag{5}$$

where g_i is the statistical weight of level i. The energy is in Rydberg units, and length is in units of the Bohr radii a_0. Figure 3 shows our calculated $E2$ and $M1$ forbidden transition rates of the $[^2D^o_{5/2,3/2}]' \to [^4S^o_{3/2}]'$ and $[^2P^o_{3/2,1/2}]' \to [^4S^o_{3/2}]'$ transitions. The scaling law for the forbidden transition rates and S are summarized from Fig. 3 and are listed in Table IV. Comparing the scaling laws in Table IV and the regular ones in Table III, many differences exist, especially in the low-Z region and for the two-electron transition, $[^2P^o_{3/2}]' \to [^4S^o_{3/2}]'$, in the high-$Z$ region. In the following, we will discuss the irregular scaling law in detail.

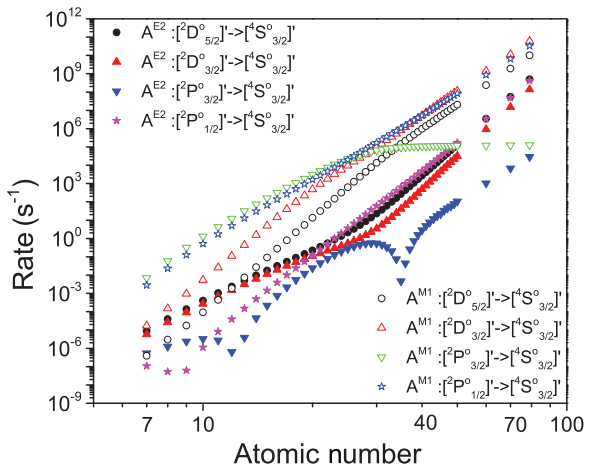

FIG. 3. (Color online) Our calculated $E2$ and $M1$ transition rates for the $[^2D^o_{5/2,3/2}]' \to [^4S^o_{3/2}]'$ and $[^2P^o_{3/2,1/2}]' \to [^4S^o_{3/2}]'$ transitions varying with Z.

E2 transition. Figure 4 shows the electric quadrupole $E2$ transition rates and line strengths S_{ij}^{E2} for the $[^2D^o_{5/2,3/2}]' \to [^4S^o_{3/2}]'$ and $[^2P^o_{3/2,1/2}]' \to [^4S^o_{3/2}]'$ transitions varying with Z. In the high-Z region, where jj coupling is appropriate, for the single-electron transitions (by comparing the chief $\mathrm{CSF}_{\{jj\}}$ of the upper and lower states), including $[^2D^o_{5/2,3/2}]' \to [^4S^o_{3/2}]$ and $[^2P^o_{1/2}]' \to [^4S^o_{3/2}]'$ transitions, the scaling laws of the rate and S agree with the corresponding scaling laws listed in Table III with $\lambda = 2$. For the two-electron transition, $[^2P^o_{3/2}]' \to [^4S^o_{3/2}]'$ (by comparing their chief $\mathrm{CSF}_{\{jj\}}$), the scaling law for S is $Z^{-2}Q^{-8}$, which totally deviates from the regular scaling law of Q^{-4} listed in Table III with $\lambda = 2$. To understand this irregular scaling law we start from the transition matrix element with the final-state wave function expanded within the framework of perturbation theory,

$$\begin{aligned}\langle\psi_i|\mathcal{O}|\psi_f\rangle &= \langle\psi_i|\mathcal{O}\big|\psi_f^{(0)}\big\rangle + \langle\psi_i|\mathcal{O}\big|\psi_f^{(1)}\big\rangle + \langle\psi_i|\mathcal{O}\big|\psi_f^{(2)}\big\rangle \\ &= \langle\psi_i|\mathcal{O}\big|\psi_f^{(0)}\big\rangle + \sum_{n\neq f}\frac{H'_{nf}}{\big(E_f^{(0)} - E_n^{(0)}\big)}\langle\psi_i|\mathcal{O}\big|\psi_n^{(0)}\big\rangle \\ &\quad + \sum_{m\neq f}\Bigg[\sum_{n\neq f}\frac{H'_{mn}H'_{nf}}{\big(E_f^{(0)} - E_m^{(0)}\big)\big(E_f^{(0)} - E_n^{(0)}\big)} \\ &\quad - \frac{H'_{mf}H'_{ff}}{\big(E_f^{(0)} - E_m^{(0)}\big)^2}\Bigg]\langle\psi_i|\mathcal{O}\big|\psi_m^{(0)}\big\rangle + \text{high orders},\end{aligned} \tag{6}$$

where $|\psi_f^{(0)}\rangle$, $|\psi_f^{(1)}\rangle$, and $|\psi_f^{(2)}\rangle$ are the zero-order, first-order perturbation, and second-order perturbation wave functions, respectively. H'_{mn} is the perturbation interaction matrix element. $\mathcal{O}$ is the interaction operator. The first term of Eq. (6) is the zero-order contribution; the second and third terms are the first-order and second-order perturbation contributions, respectively. Since $[^2P^o_{3/2}]' \to [^4S^o_{3/2}]'$ is a two-electron transition, the transition matrix element between the zero-order wave functions is forbidden, and the main contribution of the transition matrix element should arise from the first-order perturbation part, i.e., $\frac{H'_{nf}}{(E_f^{(0)} - E_n^{(0)})}\langle\psi_i|r^2|\psi_n^{(0)}\rangle$. Here H'_{nf} is the electron-electron interaction matrix element and is scaled by Q. $(E_f^{(0)} - E_n^{(0)})$ is the energy difference based on the zero-order wave function and scaled by ZQ^3. Therefore the transition matrix element can be

TABLE IV. The scaling law for the electric quadrupole $E2$ and magnetic dipole $M1$ transition rate and the line strength S summarized from Figs. 4 and 5.

Transition	Multipole	Rate of high Z	S of high Z	Rate of low Z	S of low Z
$[^2D^o_{5/2}]' \to [^4S^o_{3/2}]'$	$E2(\lambda=2)$	$\propto Z^5Q^{11}$	$\propto Q^{-4}$	$\propto Z^2Q^5$	$\propto Z^{2}$[a]
$[^2D^o_{3/2}]' \to [^4S^o_{3/2}]'$	$E2(\lambda=2)$	$\propto Z^5Q^{11}$	$\propto Q^{-4}$	$\propto Z^2Q^5$	$\propto Z^2$
$[^2P^o_{3/2}]' \to [^4S^o_{3/2}]'$	$E2(\lambda=2)$	$\propto Z^3Q^7$	$\propto Z^{-2}Q^{-8}$[b]	$\propto Z^2Q^7$	$\propto Z^2Q^{2}$[c]
$[^2P^o_{1/2}]' \to [^4S^o_{3/2}]'$	$E2(\lambda=2)$	$\propto Z^5Q^{11}$	$\propto Q^{-4}$	$\propto Z^2Q^7$	$\propto Z^2Q^2$
$[^2D^o_{5/2}]' \to [^4S^o_{3/2}]'$	$M1(\lambda=1)$	$\propto Z^3Q^9$	$\propto Q^0$	$\propto Z^4Q^9$	$\propto Z^4Q^{6}$[d]
$[^2D^o_{3/2}]' \to [^4S^o_{3/2}]'$	$M1(\lambda=1)$	$\propto Z^3Q^9$	$\propto Q^0$	$\propto Z^4Q^9$	$\propto Z^4Q^6$
$[^2P^o_{3/2}]' \to [^4S^o_{3/2}]'$	$M1(\lambda=1)$	$\propto Z^{-1}Q$	$\propto Z^{-4}Q^{-8}$[e]	$\propto Z^2Q^7$	$\propto Z^2Q^{4}$[f]
$[^2P^o_{1/2}]' \to [^4S^o_{3/2}]'$	$M1(\lambda=1)$	$\propto Z^3Q^9$	$\propto Q^0$	$\propto Z^2Q^7$	$\propto Z^2Q^4$

[a]Arising from the first-order perturbation part of Eq. (6). Here H'_{nf} is the spin-orbit interaction and is scaled by ZQ^3. $(E_f^{(0)} - E_n^{(0)})$ is the energy difference based on the zero-order wave function and is scaled by Q. Thus S is

$$\sim \left| \frac{H'_{nf}}{\left(E_f^{(0)} - E_n^{(0)}\right)} \langle \psi_i | r^2 | \psi_n^{(0)} \rangle \right|^2 \propto [(ZQ^3Q^{-1})Q^{-2}]^2 = Z^2.$$

[b]Arising from the first-order perturbation part of Eq. (6). Here H'_{nf} is the electron-electron interaction and is scaled by Q. $(E_f^{(0)} - E_n^{(0)})$ is the energy difference based on the zero-order wave function and is scaled by ZQ^3. Thus S is

$$\sim \left| \frac{H'_{nf}}{\left(E_f^{(0)} - E_n^{(0)}\right)} \langle \psi_i | r^2 | \psi_n^{(0)} \rangle \right|^2 \propto [QZ^{-1}Q^{-3}Q^{-2}]^2 = Z^{-2}Q^{-8}.$$

[c]Arising from the first-order perturbation part of Eq. (6). Here H'_{nf} is the spin-orbit interaction and is scaled by ZQ^3. $(E_f^{(0)} - E_n^{(0)})$ is the energy difference based on the zero-order wave function and is scaled by Q. Note that the transition is mainly from the minor magnetic momentum coupling since for the $E2$ transition $\Delta L = 2$ is preferred. Thus S is

$$\sim \left| \frac{H'_{nf}}{\left(E_f^{(0)} - E_n^{(0)}\right)} \langle \psi_i | r^2 \Delta E | \psi_n^{(0)} \rangle \right|^2 \propto [ZQ^3Q^{-1}Q^{-2}Q]^2 = Z^2Q^2.$$

[d]Arising from the second-order perturbation part of Eq. (6). Here H'_{nf} is the spin-orbit interaction and is scaled by ZQ^3. $(E_f^{(0)} - E_n^{(0)})$ is the energy difference based on the zero-order wave function and is scaled by Q. Note that the transition is mainly from the minor charge coupling since for the $M1$ transition $\Delta L = 1$ is preferred. Thus S is

$$\sim \left| \left[\frac{H'_{mn}H'_{nf}}{\left(E_f^{(0)} - E_m^{(0)}\right)\left(E_f^{(0)} - E_n^{(0)}\right)} - \frac{H'_{mf}H'_{ff}}{\left(E_f^{(0)} - E_m^{(0)}\right)^2} \right] \langle \psi_i | r^2 \Delta E | \psi_m^{(0)} \rangle \right|^2 \propto [ZQ^3Q^{-1}ZQ^3Q^{-1}Q^{-2}Q]^2 = Z^4Q^6.$$

[e]Arising from the second-order perturbation part of Eq. (6). Here H'_{nf} is the electron-electron interaction and is scaled by Q. $(E_f^{(0)} - E_n^{(0)})$ is the energy difference based on the zero-order wave function and is scaled by ZQ^3. Thus S is

$$\sim \left| \left[\frac{H'_{mn}H'_{nf}}{\left(E_f^{(0)} - E_m^{(0)}\right)\left(E_f^{(0)} - E_n^{(0)}\right)} - \frac{H'_{mf}H'_{ff}}{\left(E_f^{(0)} - E_m^{(0)}\right)^2} \right] \langle \psi_i | r^0 | \psi_m^{(0)} \rangle \right|^2 \propto [QZ^{-1}Q^{-3}QZ^{-1}Q^{-3}r^0]^2 = Z^{-4}Q^{-8}.$$

[f]Arising from the first-order perturbation part of Eq. (6). Here H'_{nf} is the spin-orbit interaction and is scaled by ZQ^3. $(E_f^{(0)} - E_n^{(0)})$ is the energy difference based on the zero-order wave function and is scaled by Q. Thus S is

$$\sim \left| \frac{H'_{nf}}{\left(E_f^{(0)} - E_n^{(0)}\right)} \langle \psi_i | r^0 | \psi_n^{(0)} \rangle \right|^2 \propto [ZQ^3Q^{-1}r^0]^2 = Z^2Q^4.$$

scaled by $\frac{Q}{ZQ^3}r^2 \propto \frac{Q}{ZQ^3}Q^{-2} = Z^{-1}Q^{-4}$. Accordingly, the line strength, corresponding to the square of the transition matrix element, is scaled by $Z^{-2}Q^{-8}$, and the rate is scaled by Z^3Q^7.

In the low-Z region of Fig. 4, where LS coupling is appropriate, the scaling laws of rate and S are totally different from those in the high-Z region. From the LS coupling view, the $[^2D^o_{5/2,3/2}]' \to [^4S^o_{3/2}]'$ and $[^2P^o_{3/2,1/2}]' \to [^4S^o_{3/2}]'$ transition matrix elements between the zero-order wave functions (i.e., the chief $\mathrm{CSF}_{\{LSj\}}$) are all forbidden because of their different spin quantum number. So the transition matrix elements should mainly arise from the first-order or even higher-order perturbation part of Eq. (6). Note that in the low-Z region the electron-electron interactions are dominant, and the spin-orbit interactions are treated as a perturbation. Thus H'_{nf} is the spin-orbit interaction and is scaled by ZQ^3. $(E_f^{(0)} - E_n^{(0)})$ is the energy difference based on the zero-order wave function and is scaled by Q. For $[^2D^o_{5/2,3/2}]' \to [^4S^o_{3/2}]'$ transitions, the

TABLE V. The $E2$ and $M1$ transition rates of $[^2D^o_{5/2,3/2}]' \rightarrow [^4S^o_{3/2}]'$ and $[^2P^o_{3/2,1/2}]' \rightarrow [^4S^o_{3/2}]'$ for $Z = 7$–26 for (a) this work, (b) Zeippen [5], and (c) Fischer and Tachiev [13].

Ion	$[^2D^o_{5/2}]' \rightarrow [^4S^o_{3/2}]'$		$[^2D^o_{3/2}]' \rightarrow [^4S^o_{3/2}]'$		$[^2P^o_{3/2}]' \rightarrow [^4S^o_{3/2}]'$		$[^2P^o_{1/2}]' \rightarrow [^4S^o_{3/2}]'$	
	$E2$	$M1$	$E2$	$M1$	$E2$	$M1$	$E2$	$M1$
N I	(a) 8.79[-6];	3.93[-7]	(a) 5.82[-6];	1.71[-5]	(a) 5.41[-7];	6.94[-3]	(a) 1.07[-7];	2.78[-3]
	(b) 7.08[-6];	1.94[-7]	(b) 4.59[-6];	1.56[-5]	(b) 5.38[-9];	6.58[-3]	(b) 3.27[-7];	2.71[-3]
	(c) 6.60[-6];	9.71[-7]	(c) 4.34[-6];	1.60[-5]	(c) 5.28[-10];	6.50[-3]	(c) 4.57[-7];	2.61[-3]
O II	(a) 3.94[-5];	3.02[-6]	(a) 2.59[-5];	1.50[-4]	(a) 1.27[-6];	5.87[-2]	(a) 5.28[-8];	2.35[-2]
	(b) 3.64[-5];	1.83[-6]	(b) 2.36[-5];	1.41[-4]	(b) 1.58[-9];	5.64[-2]	(b) 1.71[-6];	2.32[-2]
	(c) 3.38[-5];	7.42[-6]	(c) 2.21[-5];	1.41[-4]	(c) 1.23[-8];	5.65[-2]	(c) 1.51[-6];	2.27[-2]
F III	(a) 1.40[-4];	1.75[-5]	(a) 9.16[-5];	9.65[-4]	(a) 2.35[-6];	3.17[-1]	(a) 6.20[-8];	1.27[-1]
	(b) 1.35[-4];	1.30[-5]	(b) 8.77[-5];	9.36[-4]	(b) 2.91[-8];	3.08[-1]	(b) 6.66[-6];	1.26[-1]
	(c) 1.31[-4];	4.07[-5]	(c) 8.51[-5];	9.39[-4]	(c) 3.60[-9];	3.09[-1]	(c) 5.07[-6];	1.24[-1]
Ne IV	(a) 4.11[-4];	9.19[-5]	(a) 2.69[-4];	5.29[-3]	(a) 3.21[-6];	1.29[0]	(a) 1.14[-6];	5.19[-1]
	(b) 4.06[-4];	7.76[-5]	(b) 2.64[-4];	5.28[-3]	(b) 1.10[-6];	1.27[0]	(b) 2.64[-5];	5.21[-1]
	(c) 3.94[-4];	1.88[-4]	(c) 2.56[-4];	5.25[-3]	(c) 7.00[-8];	1.27[0]	(c) 1.60[-5];	5.10[-1]
Na V	(a) 1.05[-3];	4.39[-4]	(a) 6.81[-4];	2.57[-2]	(a) 2.73[-6];	4.30[0]	(a) 8.18[-6];	1.74[0]
	(b) 1.05[-3];	4.05[-4]	(b) 6.80[-4];	2.62[-2]	(b) 6.84[-6];	4.27[0]	(b) 8.17[-5];	1.76[0]
	(c) 1.02[-3];	7.86[-4]	(c) 6.62[-4];	2.0[-2]	(c) 1.28[-6];	4.25[0]	(c) 4.77[-5];	1.72[0]
Mg VI	(a) 2.37[-3];	1.91[-3]	(a) 1.55[-3];	1.12[-1]	(a) 6.38[-7];	1.23[1]	(a) 3.89[-5];	5.02[0]
	(b) 2.41[-3];	1.86[-3]	(b) 1.56[-3];	1.16[-1]	(b) 2.72[-5];	1.24[1]	(b) 2.20[-4];	5.11[0]
	(c) 2.35[-3];	3.04[-3]	(c) 1.52[-3];	1.15[-1]	(c) 8.82[-6];	1.23[1]	(c) 1.36[-4];	4.99[0]
Al VII	(a) 4.99[-3];	7.57[-3]	(a) 3.23[-3];	4.40[-1]	(a) 3.81[-6];	3.16[1]	(a) 1.48[-4];	1.30[1]
	(b) 5.06[-3];	7.57[-3]	(b) 3.25[-3];	4.56[-1]	(b) 8.96[-5];	3.17[1]	(b) 5.52[-4];	1.32[1]
Si VII	(a) 9.74[-3];	2.73[-2]	(a) 6.24[-3];	1.56[0]	(a) 4.40[-5];	7.35[1]	(a) 4.88[-4];	3.06[1]
	(b) 9.90[-3];	2.78[-2]	(b) 6.28[-3];	1.62[0]	(b) 2.62[-4];	7.37[1]	(b) 1.33[-3];	3.11[1]
P IX	(a) 1.80[-2];	9.12[-2]	(a) 1.13[-2];	5.03[0]	(a) 2.17[-4];	1.58[2]	(a) 1.44[-3];	6.69[1]
	(b) 1.83[-2];	9.29[-2]	(b) 1.14[-2];	5.19[0]	(b) 7.13[-4];	1.58[2]	(b) 3.14[-3];	6.79[1]
S X	(a) 3.17[-2];	2.81[-1]	(a) 1.94[-2];	1.48[1]	(a) 7.59[-4];	3.18[2]	(a) 3.92[-3];	1.38[2]
	(b) 3.24[-2];	2.86[-1]	(b) 1.95[-2];	1.51[1]	(b) 1.80[-3];	3.17[2]	(b) 7.20[-3];	1.40[2]
Cl XI	(a) 5.40[-2];	8.07[-1]	(a) 3.17[-2];	3.97[1]	(a) 2.17[-3];	6.04[2]	(a) 9.95[-3];	2.70[2]
	(b) 5.51[-2];	8.18[-1]	(b) 3.18[-2];	4.04[1]	(b) 4.19[-3];	6.00[2]	(b) 1.60[-2];	2.72[2]
Ar XII	(a) 8.92[-2];	2.18[0]	(a) 4.96[-2];	9.82[1]	(a) 5.37[-3];	1.09[3]	(a) 2.38[-2];	5.08[2]
	(b) 9.06[-2];	2.20[0]	(b) 4.94[-2];	9.91[1]	(b) 9.04[-3];	1.08[3]	(b) 3.47[-2];	5.09[2]
K XIII	(a) 1.44[-1];	5.55[0]	(a) 7.46[-2];	2.25[2]	(a) 1.19[-2];	1.87[3]	(a) 5.42[-2];	9.20[2]
	(b) 1.45[-1];	5.58[0]	(b) 7.37[-2];	2.25[2]	(b) 1.82[-2];	1.84[3]	(b) 7.32[-2];	9.18[2]
Ca XIV	(a) 2.28[-1];	1.35[1]	(a) 1.09[-1];	4.80[2]	(a) 2.41[-2];	3.08[3]	(a) 1.18[-1];	1.62[3]
	(b) 2.28[-1];	1.35[1]	(b) 1.06[-1];	4.76[2]	(b) 3.39[-2];	3.02[3]	(b) 1.51[-1];	1.61[3]
Sc XV	(a) 3.57[-1];	3.13[1]	(a) 1.54[-1];	9.62[2]	(a) 4.50[-2];	4.89[3]	(a) 2.48[-1];	2.77[3]
	(b) 3.51[-1];	3.12[1]	(b) 1.46[-1];	9.42[2]	(b) 5.89[-2];	4.76[3]	(b) 3.03[-1];	2.73[3]
Ti XVI	(a) 5.57[-1];	6.99[1]	(a) 2.13[-1];	1.82[3]	(a) 7.81[-2];	7.48[3]	(a) 5.04[-1];	4.64[3]
	(b) 5.31[-1];	6.92[1]	(b) 1.97[-1];	1.76[3]	(b) 9.43[-2];	7.23[3]	(b) 5.95[-1];	4.56[3]
V XVII	(a) 8.65[-1];	1.51[2]	(a) 2.91[-1];	3.28[3]	(a) 1.27[-1];	1.11[4]	(a) 9.96[-1];	7.63[3]
	(b) 7.98[-1];	1.49[2]	(b) 2.61[-1];	3.14[3]	(b) 1.45[-1];	1.06[4]	(b) 1.14[0];	7.45[3]
Cr XVIII	(a) 1.35[0];	3.14[2]	(a) 3.94[-1];	5.69[3]	(a) 1.93[-1];	1.58[4]	(a) 1.92[0];	1.24[4]
	(b) 1.19[0];	3.14[2]	(b) 3.29[-1];	5.30[3]	(b) 1.86[-1];	1.48[4]	(b) 2.16[0];	1.20[4]
Mn XIX	(a) 2.11[0];	6.33[2]	(a) 5.37[-1];	9.53[3]	(a) 2.75[-1];	2.19[4]	(a) 3.60[0];	1.98[4]
	(b) 1.77[0];	6.41[2]	(b) 4.14[-1];	8.68[3]	(b) 2.11[-1];	1.99[4]	(b) 3.99[0];	1.90[4]
Fe XX	(a) 3.34[0];	1.24[3]	(a) 7.39[-1];	1.56[4]	(a) 3.67[-1];	2.92[4]	(a) 6.60[0];	3.12[4]
	(b) 2.58[0];	1.29[3]	(b) 5.01[-1];	1.36[4]	(b) 1.48[-1];	2.52[4]	(b) 7.40[0];	2.97[4]

transition matrix element is scaled by $\frac{ZQ^3}{Q} r^2 \propto \frac{ZQ^3}{Q} Q^{-2} = Z$. Accordingly, the line strength is scaled by Z^2, and the rate is scaled by Z^2Q^5. For $[^2P^o_{3/2,1/2}]' \rightarrow [^4S^o_{3/2}]'$ transitions, since for the $E2$ transition $\Delta L = 2$ is preferred, the interactions from the major part, i.e., the charge coupling, are strongly forbidden, and the main contribution should come from the minor part, i.e., the magnetic momentum coupling. Thus the interaction operator $\mathcal{O}$ is $(r^2 \Delta E)$ as shown in Table III with $\lambda = 2$. The transition matrix element can be scaled by $\frac{ZQ^3}{Q}(r^2 \Delta E) \propto \frac{ZQ^3}{Q} Q^{-2} Q = ZQ$. Accordingly, the line strength is scaled by Z^2Q^2, and the rate is scaled by Z^2Q^7.

Table V lists our calculated $E2$ and $M1$ transition rates for $[^2D^o_{5/2,3/2}]' \rightarrow [^4S^o_{3/2}]'$ and $[^2P^o_{3/2,1/2}]' \rightarrow [^4S^o_{3/2}]'$ with other theoretical results [5,13] if available. For $[^2D^o_{5/2,3/2}]' \rightarrow [^4S^o_{3/2}]'$ $E2$ transitions, at $Z = 9 \sim 22$ the three theoretical results agree within a few percent, while at $Z = 7,8,23$–26

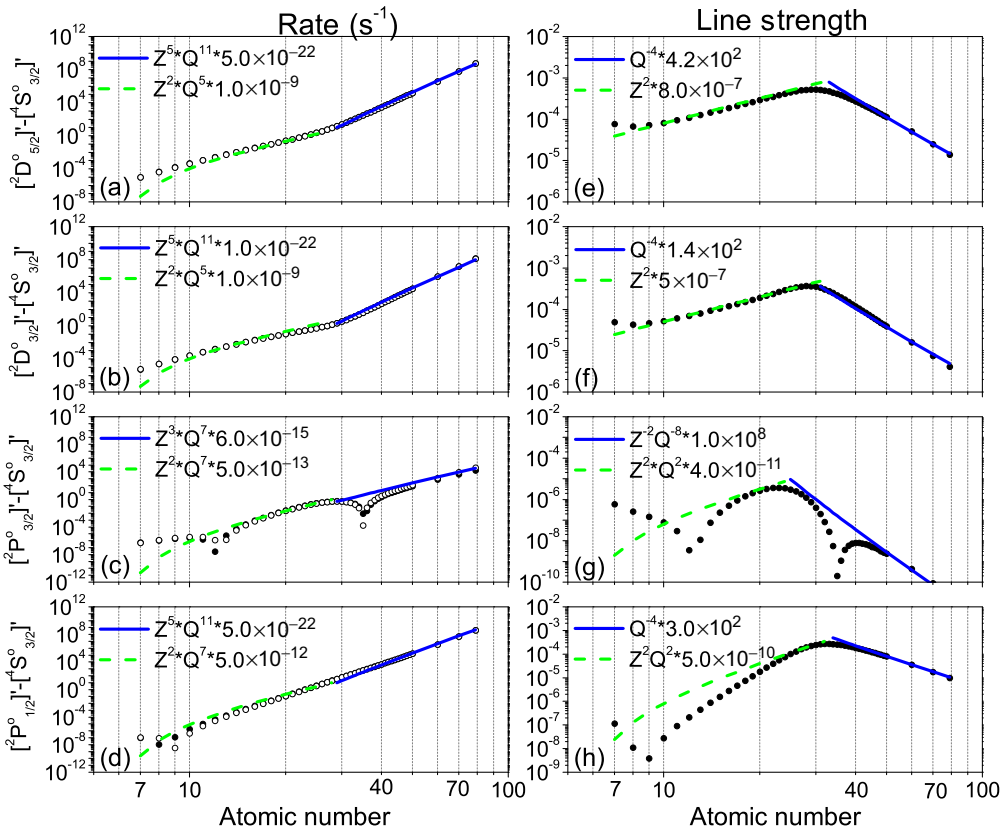

FIG. 4. (Color online) The scaling law of our calculated forbidden $E2$ transition rates and the corresponding line strengths S for (a) and (e) the $[^2D^o_{5/2}]' \to [^4S^o_{3/2}]'$ transition, (b) and (f) the $[^2D^o_{3/2}]' \to [^4S^o_{3/2}]'$ transition, (c) and (g) the $[^2P^o_{3/2}]' \to [^4S^o_{3/2}]'$ transition, and (d) and (h) the $[^2P^o_{1/2}]' \to [^4S^o_{3/2}]'$ transition.

they are only of the same magnitude. For $[^2P^o_{3/2,1/2}]' \to [^4S^o_{3/2}]'$ $E2$ transitions, at $Z > 14$ our theoretical results and Zeippen's results [5] are of the same magnitude, while at $Z \leqslant 14$ the three theoretical results differ in magnitude. Figures 4(g) and 4(h) show that in the low-Z region the value of S is tiny (smaller than 10^{-6}); therefore the convergence of the calculations for these transitions is difficult.

It is interesting to see that Figs. 4(g) and 4(h) show some interference structures around $Z = 12$ and $Z = 35$ for the $[^2P^o_{3/2}]' \to [^4S^o_{3/2}]'$ transition and around $Z = 9$ for the $[^2P^o_{1/2}]' \to [^4S^o_{3/2}]'$ transition. These structures should result from the cancellations among the terms $C^i_{r\Gamma} C^f_{r\Gamma} \langle \gamma^i_r P^i J^i M^i | \mathcal{O} | \gamma^f_r P^f J^f M^f \rangle$. More specifically, the expansion coefficients $C_{r\Gamma}$ of the initial and final states vary with Z, and the cancellations between the terms vary with Z. At certain Z, the cancellation becomes maximum, and the total transition matrix element is minimum. The structures around low Z (9 or 12) reflect the maximum cancellations between the terms consisting of $\mathrm{CSF}_{\{LSj\}}$, and the structure around $Z = 35$ reflects the maximum cancellations between the terms consisting of $\mathrm{CSF}_{\{jj\}}$, which deserve further study.

M1 transition. Figure 5 shows the magnetic dipole $M1$ transition rates and line strengths S for $[^2D^o_{5/2,3/2}]' \to [^4S^o_{3/2}]'$ and $[^2P^o_{3/2,1/2}]' \to [^4S^o_{3/2}]'$ transitions varying with Z. In the high-Z region, for the single-electron transition (by comparing their chief $\mathrm{CSF}_{\{jj\}}$), $[^2D^o_{5/2,3/2}]' \to [^4S^o_{3/2}]'$ and $[^2P^o_{1/2}]' \to [^4S^o_{3/2}]'$ transitions, the scaling laws of the rate and S agree with those listed in Table III with $\lambda = 1$. For the two-electron transition of $[^2P^o_{3/2}]' \to [^4S^o_{3/2}]'$, the scaling law of the rate is $Z^{-1}Q$. This can be explained by the second-order perturbation part of Eq. (6), i.e., $[\frac{H'_{mn} H'_{nf}}{(E^{(0)}_f - E^{(0)}_m)(E^{(0)}_f - E^{(0)}_n)} - \frac{H'_{mf} H'_{ff}}{(E^{(0)}_f - E^{(0)}_m)^2}] \langle \psi_i | \mathcal{O} | \psi^{(0)}_m \rangle$. Here H'_{mn} is the electron-electron interaction and is scaled by Q, and $(E^{(0)}_f - E^{(0)}_m)$ is the energy difference based on the zero-order wave function and is scaled by ZQ^3. The transition matrix element of the second-order perturbation part is scaled by $\frac{Q}{ZQ^3} \frac{Q}{ZQ^3} r^0 = Z^{-2}Q^{-4}$. Accordingly, the line strength is scaled by $Z^{-4}Q^{-8}$, and the rate is scaled by $Z^{-1}Q$. The scaling law means here the first-order perturbation part is unimportant compared with the second-order perturbation part.

In the low-Z region of Fig. 5, from the LS coupling point, the $[^2D^o_{5/2,3/2}]' \to [^4S^o_{3/2}]'$ and $[^2P^o_{3/2,1/2}]' \to [^4S^o_{3/2}]'$ transition matrix elements from the zero-order wave functions are all forbidden because of the different spin quantum numbers of their corresponding chief $\mathrm{CSF}_{\{LSj\}}$. So the transition matrix elements should mainly arise from the first- or second-order perturbation parts. Here H'_{nf} is the spin-orbit interaction and is scaled by ZQ^3, and $(E^{(0)}_f - E^{(0)}_n)$ is the energy difference based on the zero-order wave function and is scaled by Q. For $[^2D^o_{5/2,3/2}]' \to [^4S^o_{3/2}]'$ transitions, since for the $M1$ transition $\Delta L = 1$ is preferred, the transition from the magnetic momentum coupling is strongly forbidden, and the contribution should mainly come from the minor part, i.e., the charge coupling. Thus the interaction operator $\mathcal{O}$ is $(r^2 \Delta E)$, as shown

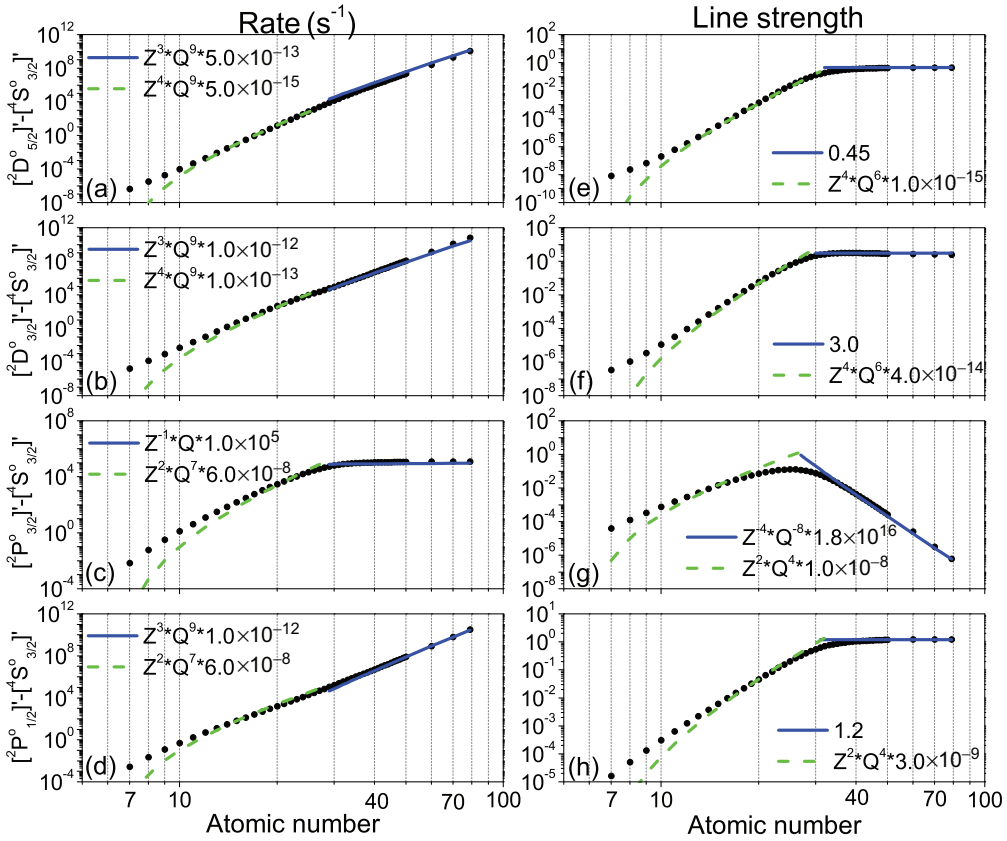

FIG. 5. (Color online) The scaling law of our calculated forbidden $M1$ transition rates and the corresponding line strengths S for (a) and (e) the $[^2D^o_{5/2}]' \to [^4S^o_{3/2}]'$ transition, (b) and (f) the $[^2D^o_{3/2}]' \to [^4S^o_{3/2}]'$ transition, (c) and (g) the $[^2P^o_{3/2}]' \to [^4S^o_{3/2}]'$ transition and (d) and (h) the $[^2P^o_{1/2}]' \to [^4S^o_{3/2}]'$ transition.

in Table III with $\lambda = 1$. According to our calculation results, S is scaled by Z^4Q^6, which can be explained by the second-order perturbation part of Eq. (6), i.e., $[\frac{ZQ^3}{Q}\frac{ZQ^3}{Q}(r^2\Delta E)]^2 \propto [\frac{ZQ^3}{Q}\frac{ZQ^3}{Q}(Q^{-2}Q)]^2 = Z^4Q^6$. Accordingly, the rate is scaled by Z^2Q^9. For $[^2P^o_{3/2,1/2}]' \to [^4S^o_{3/2}]'$ transitions, S is scaled by Z^2Q^4, which can be explained by the first-order perturbation part of Eq. (6). The transition matrix element is scaled by $\frac{ZQ^3}{Q}r^0 = ZQ^2$. Accordingly, the line strength is scaled by Z^2Q^4, and the rate is scaled by Z^2Q^7.

In Figs. 5(g) and 5(h), interference structures like those in Figs. 4(g) and 4(h) for $[^2P^o_{3/2,1/2}]' \to [^4S^o_{3/2}]'$ transitions do not appear. This is due to the different interaction operators $\mathcal{O}$ in the transition matrix element, i.e., r^2 for $E2$ and r^0 for $M1$, which leads to the different behaviors of the cancellations among the terms.

From Table V we can see that for $[^2D^o_{3/2}]' \to [^4S^o_{3/2}]'$ and $[^2P^o_{3/2,1/2}]' \to [^4S^o_{3/2}]'$ transitions the three theoretical results agree within a few percent. For the $[^2D^o_{5/2}]' \to [^4S^o_{3/2}]'$ transition, at $Z > 10$ our theoretical results and Zeippen's results [5] agree within a few percent but differ from Fischer and Tachiev's results [13] when available. At $Z \leqslant 10$ our results are larger than Zeippen's results but smaller than Fischer and Tachiev's results by several tens of percent. The reason for the large difference between the different theoretical results in the low-Z region is the tiny value of the corresponding transition matrix element (smaller than 10^{-7}), as shown in Fig. 5(e), and the absolute convergence is difficult to achieve.

Ratio. It is known that in the high-electron-density limit, the ratio of the observed forbidden line intensities of $[^2D^o_{5/2,3/2}]' \to [^4S^o_{3/2}]'$ in PNs is proportional to the radiative transition rates and the statistic weights of the ionic states when the fine-structure splittings of $[^2D^o_{5/2,3/2}]'$ are much smaller than the electron temperature of the PNs [5]. Figure 6 shows the ratio of $\{6 \times A^{(E2+M1)}([^2D^o_{5/2}]' \to [^4S^o_{3/2}]')\}/\{4 \times A^{(E2+M1)}([^2D^o_{3/2}]' \to [^4S^o_{3/2}]')\}$ and $\{4 \times A^{(E2+M1)}([^2P^o_{3/2}]' \to [^4S^o_{3/2}]')\}/\{2 \times A^{(E2+M1)}([^2P^o_{1/2}]' \to [^4S^o_{3/2}]')\}$ varying with Z. It is easy to understand the different scaling laws from low Z to high Z qualitatively from Fig. 3. More specifically, for $[^2D^o_{5/2,3/2}]' \to [^4S^o_{3/2}]'$ transitions, in the high-Z region, the $M1$ transition rates are larger than the $E2$ transition rates by several orders; thus the ratio is mainly determined by the ratio of A^{M1}. Since A^{M1} of $[^2D^o_{5/2,3/2}]'$ states in the high-Z region follows the same scaling law, i.e., $\propto Z^3Q^9$, as shown in Table IV, the corresponding ratio is nearly a constant.

In the low-Z region, for the $[^2D^o_{5/2}]'$ state, A^{M1} is larger than A^{E2}, while for the $[^2D^o_{3/2}]'$ state, A^{E2} is first larger and then becomes smaller than A^{M1}. From Figs. 4(a) and 4(b), it can be seen that $A^{E2}([^2D^o_{5/2}]' \to [^4S^o_{3/2}]')$ is nearly equal to $A^{E2}([^2D^o_{3/2}]' \to [^4S^o_{3/2}]')$, while in Fig. 3 $A^{M1}([^2D^o_{5/2}]' \to [^4S^o_{3/2}]')$ increases first slower and then faster

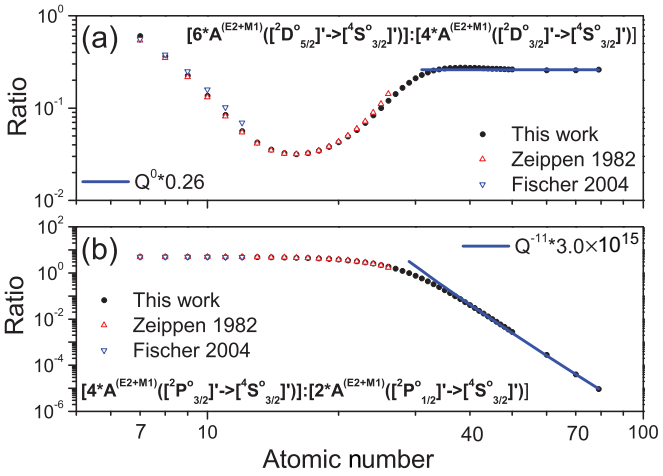

FIG. 6. (Color online) The line intensity ratio in the high-electron-density limit for (a) the $[^2D^o_{5/2}]' \to [^4S^o_{3/2}]'$ and $[^2D^o_{3/2}]' \to [^4S^o_{3/2}]'$ transitions and (b) the $[^2P^o_{3/2}]' \to [^4S^o_{3/2}]'$ and $[^2P^o_{1/2}]' \to [^4S^o_{3/2}]'$ transitions.

than $A^{M1}([^2D^o_{3/2}]' \to [^4S^o_{3/2}]')$ with increasing Z; therefore the ratio decreases first and then increases with increasing Z.

For $[^2P^o_{3/2,1/2}]'$ states, from Fig. 3 it can be seen that in the low-Z region, A^{M1} is larger than A^{E2} by several orders; thus the corresponding ratio is nearly a constant because the scaling law in this region is the same as that shown in Figs. 5(c) and 5(d). In the high-Z region, for the $[^2P^o_{3/2}]'$ state, A^{M1} is larger than A^{E2} by several orders, and A^{M1} decreases with increasing Z; therefore the ratio of $[^2P^o_{3/2,1/2}]'$ states decreases monotonously in the high-Z region with increasing Z.

Conclusion. Finally, we make the following conclusion. The energy-level structures and forbidden transition rates of the lowest five states in the $2p^3$ configuration of a N-like isoelectronic sequence have been calculated using a large-scale fully relativistic MCDF method. The scaling laws of the excitation energies for $[^2D^o_{5/2,3/2}]'$ and $[^2P^o_{3/2,1/2}]'$ states relative to the ground state $[^4S^o_{3/2}]'$ from high Z to low Z have been ascertained and are determined by the competition between the electron-electron interactions (scaled by Q) and the spin-orbit interactions (scaled by ZQ^3). The scaling laws for the fine-structure energy splittings of $[^2D^o_{5/2,3/2}]'$ and $[^2P^o_{3/2,1/2}]'$ states in the high-Z region have been given.

The general scaling law for the multipole transition rates derived from a single-particle model is presented in Table III. The scaling laws of $E2$ and $M1$ transition rates for $[^2D^o_{5/2,3/2}]' \to [^4S^o_{3/2}]'$ and $[^2P^o_{3/2,1/2}]' \to [^4S^o_{3/2}]'$ transitions have been concluded from our calculation results. In general, the scaling laws for the one-electron transitions in the high-Z region are consistent with the scaling laws listed in Table III, while for the two-electron transition in the high-Z region, the contributions of the first- or second-order perturbation parts of Eq. (6) are dominant and the scaling laws differ from those in Table III. In the low-Z region, the scaling law of the transition matrix has been determined by the first-order perturbation part of Eq. (6) since the transition matrix between the zero-order wave function in LS coupling is forbidden because of the different spin quantum number. The ratios of $\{6 \times A^{(E2+M1)}([^2D^o_{5/2}]' \to [^4S^o_{3/2}]')\}/\{4 \times A^{(E2+M1)}([^2D^o_{3/2}]' \to [^4S^o_{3/2}]')\}$ and $\{4 \times A^{(E2+M1)}([^2P^o_{3/2}]' \to [^4S^o_{3/2}]')\}/\{2 \times A^{(E2+M1)}([^2P^o_{1/2}]' \to [^4S^o_{3/2}]')\}$ of the sequence have been presented, and the scaling laws in the high-Z region have been given. Our calculated atomic data and the scaling law are expected to be useful for future applications of astrophysics and plasma physics.

ACKNOWLEDGMENTS

This work is supported by the National Basic Research Program of China (Grants No. 2010CB922900, No. 2011CB921501, and No. 2013CB922200), the National Science Foundation of China (Grants No. 10933001, No. 11275029, and No. 11274035), the Foundation for the Development of Science and Technology of the Chinese Academy of Engineering Physics (Grants No. 2013A0102005, and No. 2011A0102007), the Ministry of Science and Technology of Ministry of Education of China, The Key Grant Project of the Chinese Ministry of Education (No. 306020), The National High-Tech ICF committee of China, and the Yin-He Super-computer Center.

APPENDIX: ESTIMATION OF TRANSITION RATE

The Hamiltonian of atoms in the presence of a radiation field can be written as (in this appendix SI units are used if not otherwise specified)

$$H = H_a + H_{em} + H_{a,em}. \tag{A1}$$

H_a is the Hamiltonian of the isolated atom (or ion) with N electrons and can be expressed as (here atomic units are used)

$$H_a = \sum_{n=1}^{N} \left(-\frac{1}{2}\nabla_n^2 - \frac{Z}{r_n} + \sum_{m>n}^{N} \frac{1}{r_{nm}} + \frac{\alpha^2 Z}{2} \frac{l_n \cdot \mathbf{s}_n}{r_n^3} \right), \tag{A2}$$

where no relativistic effects except the spin-orbit interactions are included. α is the fine-structure constant. $H_{em} = \sum_{k,\lambda} (a^+_{k\lambda} a_{k\lambda} + \frac{1}{2})\hbar\omega$ is the Hamiltonian of the radiation field. $H_{a,em}$ is the interaction between the atom and the radiation field. In order to understand the scaling law quantitatively, it is convenient to express the interaction Hamiltonian in a nonrelativistic form,

$$H_{a,em} = -\sum_a \left(\frac{e}{mc} \mathbf{A} \cdot \mathbf{p}_a + \frac{e\hbar}{2mc} \vec{\mu}_a \cdot \mathbf{curlA} - \frac{e^2}{2mc^2} A^2 \right), \tag{A3}$$

where $\vec{\mu}_a$ is the magnetic moment. $\mathbf{A}$ is the vector potential of an electromagnetic wave and is the vector solution of the wave equation: $(\nabla^2 + k^2)\mathbf{A} = 0$. For convenience, $\mathbf{A}$ is expanded by electric or magnetic multipole fields, which form a complete set. The vector solutions of the wave equation are divided into two parts, electric multipoles and magnetic multipoles, as follows:

$$\begin{aligned} \mathbf{A}^M_{cJ} &= \frac{\sqrt{2}}{\sqrt{J(J+1)}} \frac{1}{\hbar} \mathbf{curlL} u^M_J(kr), \\ \mathbf{A}^M_{mJ} &= \frac{\sqrt{2}}{\sqrt{J(J+1)}} \frac{k}{\hbar} \mathbf{L} u^M_J(kr). \end{aligned} \tag{A4}$$

Here $u_l^m = j_l(kr)Y_l^m(\theta,\phi)$ is the scalar solutions of the wave function in vacuum $(\nabla^2 + k^2)u = 0$. $j_l(kr)$ is the spherical Bessel function, and $Y_l^m(\theta,\phi)$ is the spherical harmonics function. **L** is the orbital angular momentum operator. The last term including A^2 in Eq. (A3) is neglected in the following discussion since this term is relative to the two-photon process and is supposed to be unimportant in the one-photon process. An estimate of the vector potential near the origin ($kr \ll l$) is obtained by using the approximations that $j_l(kr) \cong \frac{(kr)^l}{(2l+1)!!}$ with $(kr) \ll l$ and $\mathbf{curl} \approx 1/r$. Assuming $\mathbf{L} \approx 1$, the electric multipole and magnetic multipole fields are estimated as

$$|A_{c\lambda}| \cong k(kr)^{\lambda-1}, \tag{A5}$$

$$|H_{c\lambda}| = \mathbf{curlA}_c^\lambda \cong k^2(kr)^\lambda, \tag{A6}$$

$$|A_{m\lambda}| \cong k(kr)^\lambda, \tag{A7}$$

$$|H_{m\lambda}| = \mathbf{curlA}_m^\lambda \cong k^2(kr)^{\lambda-1}. \tag{A8}$$

In Eqs. (A6) and (A8) we use the relation $\mathbf{curlcurl} = k^2$ from the wave equation $(\mathbf{curlcurl} - k^2)\mathbf{A} = 0$.

On the other hand, the electromagnetic field can be quantized as a sum of photons of definite multipolarity. The general field can be expanded as

$$\mathbf{A} = \sum_\tau (q_\tau \mathbf{A}_\tau + q_\tau^\dagger \mathbf{A}_\tau^*), \tag{A9}$$

where $\mathbf{A}_\tau$ are the multipole fields and q_τ are their amplitudes to be quantized. τ represents all the quantum numbers k, J, M, π. The quantized amplitudes are

$$q_\tau = \sqrt{\frac{2\pi\hbar}{\omega_\tau}} c a_\tau, \tag{A10}$$

and a_τ are annihilation operators. The interaction Hamiltonian can be expanded as

$$\mathbf{A}\cdot\mathbf{p}_a = \sqrt{2\pi\hbar}\sum_\tau \frac{1}{\sqrt{\omega_\tau}}[\mathbf{A}_\tau\cdot\mathbf{p}_a a_\tau + \mathbf{A}_\tau^*\cdot\mathbf{p}_a a_\tau^\dagger],$$

$$\mu_a\vec{\sigma}\cdot\mathbf{H} = \mu_a\sqrt{2\pi\hbar}c\vec{\sigma}\cdot\sum_\tau \frac{1}{\sqrt{\omega_\tau}}[\mathbf{curlA}_\tau a_\tau + \mathbf{curlA}_\tau^* a_\tau^\dagger]. \tag{A11}$$

In the independent particle model, $\mathbf{p}_a$ is the momentum operator of a single particle and can be estimated as

$$\begin{aligned}\langle\psi_f|\mathbf{p}_a|\psi_i\rangle &= m\frac{d}{dt}\langle\psi_f|r_a|\psi_i\rangle = \frac{m}{i\hbar}\langle\psi_f|r_\alpha H - Hr_a|\psi_i\rangle \\ &= \frac{m}{i\hbar}(E_i - E_f)\langle\psi_f|r_a|\psi_i\rangle \approx im\omega r,\end{aligned} \tag{A12}$$

where $|\psi_i\rangle$ and $|\psi_f\rangle$ represent the initial- and final-state wave functions, respectively.

Then we obtain

$$\frac{e}{m}\sqrt{\frac{2\pi\hbar}{\omega}}\mathbf{A}_{c\lambda}\cdot\mathbf{p} \approx C\frac{mc}{\hbar}\sqrt{k}(kr)^\lambda \tag{A13}$$

for electric multipole charge coupling,

$$\frac{e\hbar}{2m}\sqrt{\frac{2\pi\hbar}{\omega}}\mu\vec{\sigma}\cdot\mathbf{H}_{c\lambda} \approx C\frac{\sqrt{k}}{r}(kr)^{\lambda+1} \tag{A14}$$

for electric multipole magnetic momentum coupling,

$$\frac{e\hbar}{2m}\sqrt{\frac{2\pi\hbar}{\omega}}\mu\vec{\sigma}\cdot\mathbf{H}_{c\lambda} \approx C\frac{\sqrt{k}}{r}(kr)^{\lambda} \tag{A15}$$

for magnetic multipole magnetic momentum coupling, and

$$\frac{e}{m}\sqrt{\frac{2\pi\hbar}{\omega}}\mathbf{A}_{c\lambda}\cdot\mathbf{p} \approx C\frac{mc}{\hbar}\sqrt{k}(kr)^{\lambda+1} \tag{A16}$$

for magnetic multipole charge coupling, where $C = \frac{e}{m}\sqrt{\frac{2\pi\hbar^3}{c}}$.

According to Fermi's golden rule, the transition probabilities A of electric multipoles (E_c^λ and E_m^λ) and magnetic multipoles (H_c^λ and H_m^λ) are proportional to the transition matrix element $\langle\psi_f|H_{\rm int}|\psi_i\rangle$, namely,

$$A(E_c^\lambda) \propto k^{2\lambda+1}|\langle\psi_f|r^\lambda|\psi_i\rangle|^2, \tag{A17}$$

$$A(E_m^\lambda) \propto k^{2\lambda+1}|\langle\psi_f|r^{\lambda-1}(kr)|\psi_i\rangle|^2, \tag{A18}$$

$$A(H_c^\lambda) \propto k^{2\lambda+1}|\langle\psi_f|r^\lambda(kr)|\psi_i\rangle|^2, \tag{A19}$$

$$A(H_m^\lambda) \propto k^{2\lambda+1}|\langle\psi_f|r^{\lambda-1}|\psi_i\rangle|^2, \tag{A20}$$

where $k = \nu/c$ is proportional to the transition frequencies (i.e., the transition energy).

[1] M. J. Seaton, Adv. At. Mol. Phys. **4**, 331 (1968).
[2] D. E. Osterbrock, *Astrophysics of Gaseous Nebulae* (Freeman, San Francisco, 1974).
[3] U. Feldman, Phys. Scr. **24**, 681 (1981).
[4] S. Sudkewer, Phys. Scr. **23**, 72 (1981).
[5] C. J. Zeippen, Mon. Not. R. Astron. Soc. **198**, 111 (1982).
[6] W. Eissner, M. Jones, and H. Nussbaumer, Comput. Phys. Commun. **8**, 270 (1974).
[7] R. H. Garstang, Opt. Pura Apl. **5**, 192 (1972).
[8] B. C. Fawcett, At. Data Nucl. Data Tables **22**, 473 (1978).
[9] K. T. Cheng, Y. K. Kim, and J. P. Desclaux, At. Data Nucl. Data Tables **24**, 111 (1979).
[10] A. K. Bhatia and H. E. Mason, Mon. Not. R. Astron. Soc. **190**, 925 (1980).
[11] A. K. Bhatia and H. E. Mason, Astron. Astrophys. **83**, 380 (1980).
[12] M. Eidelsberg, F. Crifo-Magnnat, and C. J. Zeippen, Astron. Astrophys. Suppl. Ser. **43**, 455 (1981).
[13] C. F. Fischer and G. Tachiev, At. Data Nucl. Data Tables **87**, 1 (2004).

[14] C. F. Fischer, T. Brage, and P. Jönsson, *Computational Atomic Structure: An MCHF Approach* (IOP, Bristol, UK, 1997).
[15] X. L. Wang, W. L. Lu, X. Gao, and J. M. Li, Chin. Phys. Lett. **26**, 043101 (2009).
[16] S. H. Chen, B. Qing, and J. M. Li, Phys. Rev. A **76**, 042507 (2007).
[17] X. Y. Han, X. Gao, D. L. Zeng, J. Yan, and J. M. Li, Phys. Rev. A **85**, 062506 (2012).
[18] D. Layzer and J. Bahcall, Ann. Phys. (N.Y.) **17**, 177 (1962).
[19] A. W. Weiss and Y.-K. Kim, Phys. Rev. A **51**, 4487 (1995).
[20] M. J. Vilkas, Y. Ishikawa, and K. Koc, Phys. Rev. A **60**, 2808 (1999).
[21] F. A. Parpia, C. F. Fischer, and I. P. Grant, Comput. Phys. Commun. **94**, 249 (1996).
[22] P. Jönsson, X. He, C. Froese Fischer, and I. P. Grant, Comput. Phys. Commun. **177**, 597 (2007).
[23] P. Jönsson and J. Bieroń, J. Phys. B **43**, 074023 (2010).
[24] P. Jönsson, S. Verdebout, and G. Gaigalas, J. Phys. B **45**, 165002 (2012).
[25] J. Ekman, J. Grumer, H. Hartman, and P. Jönsson, J. Phys. B **46**, 095001 (2013).
[26] I. P. Grant, *Relativistic Quantum Theory of Atoms and Molecules* (Springer, New York, 2006).
[27] M. H. Chen, K. T. Cheng, and W. R. Johnson, Phys. Rev. A **47**, 3692 (1993).
[28] T. Brage and C. F. Fischer, Phys. Scr. **T47**, 18 (1993).
[29] I. P. Grant, Adv. Phys. **19**, 747 (1970).
[30] W. Ong and S. T. Manson, Phys. Rev. A **19**, 688 (1979).
[31] M. R. Godefroid, Phys. Scr. **T65**, 70 (1996).
[32] J. Bieroń, P. Jönsson, and C. Froese Fischer, Phys. Rev. A **60**, 3547 (1999).
[33] C. F. Fischer, M. Godefroid, and J. Olsen, J. Phys. B **30**, 1163 (1997).
[34] M. R. Godefroid, C. F. Fischer, and P. Jönsson, J. Phys. B **34**, 1079 (2001).
[35] C. F. Fischer, Phys. Scr. **T134**, 014019 (2009).
[36] B. Qing, C. Cheng, X. Gao, X. L. Zhang, and J. M. Li, Acta Phys. Sin. **59**, 4547 (2010) [in Chinese].
[37] X. L. Zhang, C. Cheng, X. Gao, and J. M. Li, Chin. Phys. Lett. **27**, 033101 (2010).
[38] C. Cheng, X. L. Zhang, X. Gao, B. Qing, and J. M. Li, J. Phys. B **43**, 105001 (2010).
[39] X. Gao and J. M. Li, Chin. Phys. Lett. **27**, 063101 (2010).
[40] C. Cheng, X. Gao, B. Qing, X. L. Zhang, and J. M. Li, Chin. Phys. B **20**, 033103 (2011).
[41] J. B. Mann and W. R. Johnson, Phys. Rev. A **4**, 41 (1971).
[42] I. P. Grant and B. J. McKenzie, J. Phys. B **13**, 2671 (1980).
[43] R. D. Cowan, *The Theory of Atomic Structure and Spectra* (University of California Press, Berkeley, 1981), p. 255.
[44] The scaled Schrodinger equation for a hydrogenlike system is $[-\frac{1}{2}(\frac{d^2}{d\bar{r}^2} - \frac{l(l+1)}{\bar{r}^2}) - \frac{1}{\bar{r}}]\phi(\bar{r}) = \bar{\epsilon}\phi(\bar{r})$. Here $\bar{r} = rQ$, $\bar{\epsilon} = \frac{\epsilon}{Q^2}$. Thus $r = \bar{r}/Q \propto Q^{-1}$.
[45] B. C. Fawcett, At. Data Nucl. Data Tables **16**, 135 (1975).
[46] S. Debenedetti, *Nuclear Interactions*, 3rd ed. (Wiley, New York, 1964), p. 264.